Impact of synthesis temperature and precursor ratio on the crystal quality of MOCVD WSe₂ monolayers

Annika Grundmann^{1*}, Yannick Beckmann², Amir Ghiami¹, Minh Bui^{3,4}, Beata Kardynal^{3,4},
Lena Patterer⁵, Jochen Schneider⁵, Tilmar Kümmell², Gerd Bacher², Michael Heuken^{1,6},
Holger Kalisch¹, Andrei Vescan¹

¹Compound Semiconductor Technology, RWTH Aachen University, 52074 Aachen, Germany ²Werkstoffe der Elektrotechnik and CENIDE, University of Duisburg-Essen, 47057 Duisburg, Germany

³Peter Grünberg Institute (PGI-9), Forschungszentrum Jülich, 52425 Jülich, Germany

⁴Department of Physics, RWTH Aachen University, 52074 Aachen, Germany

⁵Materials Chemistry, RWTH Aachen University, 52074 Aachen, Germany

⁶AIXTRON SE, 52134 Herzogenrath, Germany

ABSTRACT

Structural defects in transition metal dichalcogenide (TMDC) monolayers (ML) play a significant role in determining their (opto)electronic properties, triggering numerous efforts to control defect densities during material growth or by post-growth treatments. Various types of TMDC have been successfully deposited by MOCVD (metal-organic chemical vapor deposition), which is a wafer-scale deposition

^{*}grundmann@cst.rwth-aachen.de; phone +49 241 80-27748; https://www.cst.rwth-aachen.de/

technique with excellent uniformity and controllability. However, so far there are no findings on the extent to which the incorporation of defects can be controlled by growth parameters during MOCVD processes of TMDC. In this work, we investigate the effect of growth temperature and precursor ratio during MOCVD of tungsten diselenide (WSe₂) on the growth of ML domains and their impact on the density of defects. The aim is to find parameter windows that enable the deposition of WSe₂ ML with high crystal quality, i.e. a low density of defects. Our findings confirm that the growth temperature has a large influence on the crystal quality of TMDC, significantly stronger than found for the W to Se precursor ratio. Raising the growth temperatures in the range of 688 °C to 791 °C leads to an increase of the number of defects, dominating photoluminescence (PL) at low temperatures (5.6 K). In contrast, an increase of the molar precursor ratio (DiPSe/WCO) from 1,000 up to 100,000 leads to less defect-related PL at low temperatures.

Keywords: metal-organic chemical vapor deposition, 2D materials, transition metal dichalcogenides, MOCVD, defects, chalcogen vacancies, growth parameters, WSe₂

1. INTRODUCTION

Two-dimensional (2D) materials, particularly transition metal dichalcogenides (TMDC), feature unique (opto)electronic properties such as direct bandgaps in the visible photon energy region, large absorption coefficients and high carrier mobilities [1–3], which make them promising candidates for next-generation (opto)electronics. Photodetectors, photodiodes, light-emitting diodes (LED) as well as proof-of-concept transistors have already been demonstrated [4–12]. However, their (opto)electronic performance is strongly influenced by the density of structural defects such as vacancies and substitutional impurities [13–19] and thus far below theoretical predictions [20]. Those defects can trap

free charge carriers and localize / trap excitons, leading to nonradiative Shockley-Read-Hall recombinations (SRH). Compared to conventional bulk semiconductors, the reduced dimensionality of 2D-TMDC leads to a stronger interaction between defects and charge carriers / excitons due to a strong confinement of the electron wavefunction [13]. Among all intrinsic defects, chalcogen vacancies have the lowest formation energy and thus are considered to be the most abundant defects in 2D-TMDC [21–26]. In the case of WSe₂, we expect Se vacancies (V_{Se}) to be the dominant species [24,25,27,28]. V_{Se} introduce acceptor states in the bandgap of WSe₂ monolayer (ML) acting as electron traps ^[29,30]. Electrons can be captured from the conduction band via Auger processes or/and phonon assisted processes [20,29,31]. Free excitons generated by optical excitation can localize / be trapped at these defect states on a very fast time scale (~ 1 ps) [29,31,32]. Radiative recombination leads to photoluminescence (PL) emission at energies lower than the free exciton transition energy X^{A [13]}. These excitons are also called defect-bound excitons. The emission of defect-bound excitons X^b is highly dependent on the temperature, usually dominating PL emission at low temperatures ($\leq 77 \text{ K}$) [33]. At higher temperatures, defect-bound excitons can be thermally activated (thermal activation energy: 37 - 43 meV $^{[33,34]}$) into continuum to be captured by competing nonradiative recombination centres or recombine radiatively as free excitons ^[20,35]. Because the defect-assisted nonradiative recombination is much faster than the radiative recombination of A excitons (XA) in ML WSe₂ (0.254 ns⁻¹ at RT) [36], nonradiative recombination dominates, resulting in low quantum yield (QY). At high exciton densities (~ 10⁹ cm⁻¹ ²), exciton-exciton annihilation (EEA) processes become dominant in the exciton decay ^[20]. Such second-order processes reduce the fraction of radiative exciton recombination further, once more resulting in low photoluminescence quantum yield (PLQY), e.g. 3 % for ML WSe₂ at RT ^[31,37,38]. The excitons collision probability which leads to EEA is defined by the exciton diffusion length, which can be reduced in the presence of localizing defect states [20,39,40]. Thus, a certain density of defects is expected not to degrade PL emission but suppress EEA processes at sufficient excitation densities ^[20]. It is therefore important to understand the mechanisms by which the amount of defects and thus the crystal quality can be controlled during growth in order to provide an effective way to boost the performance of light-emitting devices based on 2D-TMDC. A theoretical study of point defects in ML MoS₂ has shown that the density of S vacancies increases with growth temperature leading to a S vacancy concentration of about 1 × 10⁹ cm⁻² at 1200 K ^[41]. In some other works, it was also shown that the concentration of chalcogen vacancies can be controlled by growth parameters such as growth rate and chalcogen to metal precursor ratio ^[42–45]. Due to the tight correlation between growth conditions and crystal quality of 2D-TMDC ^[46], it is of great importance to investigate the impact of various growth parameters on the density of defects. MOCVD is particularly suitable for this due to its high reproducibility, controllability and excellent uniformity. In this work, we concentrate on varying growth temperature and precursor ratio of large-scale WSe₂ samples deposited by MOCVD and analyzing the impact of those growth parameters on the crystal quality.

2. EXPERIMENTAL DETAILS

WSe₂ was deposited by MOCVD using tungsten hexacarbonyl (WCO) 99.9 % and diisopropylselenide (DiPSe) 99.9999 % (both Dockweiler Chemicals) as precursors in a commercial AIXTRON reactor in 10 × 2" configuration on sapphire (0001) substrates with a nominal offcut of 0.2° towards m-plane. A major advantage of the selenium precursor DiPSe used in this work is that, in contrast to H₂Se, it is not toxic and in addition, parasitic gas-phase prereactions can be significantly reduced. Following a substrate prebake step at 1050 °C for 15 min in hydrogen atmosphere ^[47], WSe₂ growth processes were carried out at 30 hPa total pressure in N₂. In our first experiment (sample series I), the impact of the synthesis temperature on the defectiveness of WSe₂ was investigated. Following the 15 min substrate

prebake step, the deposition was performed at six different surface temperatures between 537 °C and 791 °C in deposition processes of 45 min each. During growth the WCO flow was kept constant at 259 nmol/min and the DiPSe flow at 259 μ mol/min. An overview of the samples can be found in table 1.

To investigate the impact of the precursor ratio (sample series II), the DiPSe flow was increased at different WCO flows, at a constant growth temperature of 587 °C. Sample series II encompasses three different DiPSe/WCO molar ratios: 1,000, 10,000 and 100,000. Sample characteristics can be found in table 2. The intention for the higher DiPSe/WCO ratios was to reduce the density of defects. Our previous investigations have shown that at high precursor ratios, the nucleation density and domain size increase, leading to an overall increased surface coverage. Therefore, to obtain comparable coverage and average domain sizes for the three precursor ratio samples, the growth time was shortened to 15 min for the DiPSe/WCO ratio of 100,000 (see table 2). All samples were characterized using atomic force microscopy (AFM), scanning electron microscopy (SEM), Raman spectroscopy and photoluminescence (PL) / reflectance spectroscopy. The images obtained by SEM were analyzed with the image processing program ImageJ to determine the surface coverage of the samples. Raman measurements (Renishaw in Via) were performed in air with a 532 nm excitation wavelength with a laser power density of about 0.5 mW/cm². The PL measurements were performed in air at room temperature (RT) and under vacuum at 5.6 K with excitation wavelengths of 532 nm and 442 nm, respectively. Due to a different measurement set-up, the laser spot size for the measurements at RT was smaller than for the measurement at 5.6 K, thus the power density of the set-up at RT was in the range of a few MW/cm², whereas the power density at 5.6 K was in the range of W/cm². Reflectance measurements were carried out at 9.5 K with a 730 nm LED in a confocal setup with a 20 µm pinhole. For the chemical analysis, X-ray photoelectron spectroscopy (XPS) measurements were carried out in an AXIS Supra (Kratos Analytical Ltd.) using monochromatic Al K_{α} radiation. To avoid charging effects, a charge neutralizer (low-energy, electron-only source) was used during data acquisition. The binding energy (BE) scale was calibrated with respect to the Al 2p signal of the sapphire substrate at BE = 74.0 eV. Chemical quantification and spectra deconvolution were performed by using the XPSPeak software, subtracting a Shirley background [48], employing the sensitivity factors provided by the manufacturer, and using a Voigt-type line shape.

3. RESULTS AND DISCUSSIONS

The effect of MOCVD growth temperature on the crystal quality of WSe₂ was explored in sample series I. As already stated above, we investigated surface temperatures ranging from 537 °C to 791 °C to study the influence of temperature on the generation of defects ^[28]. This temperature range was selected based on optimization in prior work. Below 537 °C, no crystalline layers could be deposited, whereas above 791 °C, parasitic carbon deposition becomes dominant. One aspect of surface temperature impact is related to thermodynamics (activation energy for defect formation) ^[25,27]. As the chemical potential of the chalcogens decreases with increasing growth temperature in the chalcogenrich limit ^[27,28] (leading to a reduction of the formation energy of V_{Se} ^[25]), we expect the V_{Se} density to rise with increasing growth temperature. The other aspect is of kinetic nature. An increase in the surface temperature leads to a decrease in adatom sticking, especially of the volatile element Se ^[49]. This trend in favor of vacancy formation is enhanced by a significantly increased equilibrium vapor pressure of Se over WSe₂ ^[45].

Figure 1a shows SEM images of the surfaces of the samples. All samples exhibit the typical triangular shape of nuclei. As can be seen in figure 1b, increasing the surface temperature from 537 °C to 791 °C leads to a decrease in ML coverage from about 70 % to 45 % while the lateral domain size increases from 26 nm to 95 nm, indicating a larger critical nucleus size and thus a smaller nucleation density. This trend is consistent with thermodynamic calculations of the nucleation process in literature ^[50] as well as experimental observations ^[45,51,52]. For temperatures above 587 °C, the bilayer (BL) coverage is negligibly small and constant below 2 %. In these cases, the domain size is most likely sufficiently small (and the diffusion length of adatoms large enough) to allow adatoms to reach the domain edges before contributing to BL growth. The thickness of the nuclei was determined by AFM measurements. Figure 1c and d show exemplarily an AFM measurement of the surface of the 738 °C sample with the corresponding measured height profile. The nucleus height of around 617 pm corresponds to that expected for ML WSe₂ ^[53].

Figure 2 displays the Raman spectra of sample series I. The peak at 250 cm⁻¹ is associated with the two first-order Raman modes E^{1}_{2g} and A_{1g} of WSe₂ (see figure 2a), which have practically the same frequency, preventing a clear identification of their individual contributions ^[54]. The peak at 260 cm⁻¹ can be assigned to the 2LA(M) mode ^[55]. The predominant ML nature of the nuclei is confirmed by the absence of B^{1}_{2g} Raman peaks (~ 310 cm⁻¹) in the inset of figure 2a. The B^{1}_{2g} corresponds to an interlayer breathing mode, which only becomes Raman-active for a few-layer thickness due to van der Waals forces between adjacent layers ^[55]. Because Raman spectroscopy only probes the vibrational properties and the perturbation in the crystal lattice, it is insensitive for detecting the relatively small densities of defects in TMDC (e.g. $\approx 10^9$ cm⁻² at 1200 K) ^[41,56]. However, the much lower intensity of the peak at 250 cm⁻¹ for the samples with a growth temperature of 537 °C and 791 °C (see figure 2b) could be an indication for an inferior crystal quality as deviations from the ideal crystal lattice break

the symmetry of the WSe₂ ML and reduce the spectral intensity of the out-of-plane A_{1g} mode ^[29]. It should be noted that this difference in intensity of the peak at 250 cm⁻¹ was reproducible.

To obtain a deeper insight into the impact of the surface temperature on the crystal quality of the WSe₂ domains, (low-temperature) PL and XPS measurements were performed. Figure 3 shows the PL spectra measured at 5.6 K and RT. The insets display the PL peak position as a function of the excitation power density. All spectra are normalized to the intensity of the sapphire PL located at 1.79 eV [57]. Due to the high excitonic binding energies of TMDC (240 meV for WSe₂ on sapphire [58]), PL signals are dominated by excitonic transitions up to RT. The peak denoted as X^b in the spectra measured at 5.6 K is significantly red-shifted compared to the expected position of the A exciton emission of WSe₂ at around 1.72 eV at low temperatures ^[34,59,60]. In accordance with previous reports on PL from ML WSe₂, this peak corresponds to excitons localized at defects ^[33,34,61]. The samples deposited at 738 °C and 791 °C exhibit the highest defect-related PL intensity, suggesting a high defect density. One could expect a lower defect-related PL for those samples deposited at higher growth temperatures because of their smaller nucleation density and thus less contributions of defective domain edges. In general, the characterization methods used in this work, e.g. SEM and PL, do not provide information on the exact type and origin of defect luminescence. However, we can conclude on the basis of our results that there is no dominant contribution by edge defects. Furthermore, these two samples show a slight variation in terms of intensity and peak position, which will be explained later by XPS results. The inset in figure 3a shows the power dependence of the PL peak position at 5.6 K. Defect state filling is expected to saturate at high excitation power densities. This is leading to a nonlinear dependence of the X^b intensity on excitation power [33,61-63]. Although the PL peak position blue-shifts with increasing power density for all samples, the position of the PL peak is still in the spectral region of localized exciton emission even at the highest power density. This suggest that either the power density is not sufficient to completely saturate the defects or different defects are involved and their relative contribution changes with increasing power density.

At RT, the X^b peak no longer dominates since the thermal energy is sufficient to delocalize the excitons in real space [33]. However, electron capture by defects in defect-assisted nonradiative recombination processes can still occur by phonon-assisted processes [31]. The PL peak positions at RT are consistent with the reported literature value of the A exciton transition in WSe₂, experimentally predicted to be at around 1.65 eV on sapphire [45,58,59,63,64]. The slight asymmetry is typically attributed to additional contributions from trions (X') at lower energies [59,64,65]. With increasing excitation power, many-body effects lead to a red-shift of the PL peak position [66]. suggesting the recombination of free excitons at RT. The comparatively low PL emission at RT and 5.6 K for the 537 °C sample suggests the presence of a very high density of structural defects or strong deviations from stoichiometry. Considering the expected position of the PL peak of the A exciton at 1.65 eV, the samples deposited at 587 °C and 636 °C show the strongest emission intensity in this range at RT. However, the sample deposited at 587 °C exhibits the lowest defect-induced emission at 5.6 K, suggesting the lowest defect density.

Figure 4a and b display the chemical composition analysis via XPS for all samples of the growth temperature series I with the characteristic W 4f and W 3p3/2, as well as the Se 3d core levels, agreeing with previous reports ^[67,68]. Deviations from the ideal line shape such as the comparatively large full width at half maximum (FWHM) values of the W 4f and S3d core levels and additional peaks indicate changes in crystal quality which could be attributed for example to the existence of additional species. The increase of the FWHM of the W 4f7/2 and Se 3d5/2 peaks with temperature (see figure 4c) confirms that the growth temperature has, as expected, a strong impact on the crystal quality of the WSe₂ ML domains. Consequently, the sample with a growth temperature of 791 °C features the

highest value of the FWHM of the W 4f7/2 and Se 3d5/2 peaks. The Se:W ratios obtained from the quantitative analysis are shown in figure 4d. Apart from the 791 °C sample, the stoichiometric values are within 5% of the nominal value of 2.0. As the error on the measured stoichiometries is in the 3-5% range, it is not possible to quantitatively correlate the (opto)electronic properties to the stoichiometry determined by XPS ^[69]. Nevertheless, due to the large FWHM of the W 4f and W 3p3/2, as well as the Se 3d core levels, the strongest defect-induced PL emission is expected for the 791 °C sample, which was indeed confirmed in the low-temperature-PL measurement given in figure 3a. Furthermore, this suggests that the defect-induced PL emission is related to point defects and not domain edges as the average domain size is highest and coverage lowest for this growth temperature. In order to get more insight into the chemical composition of the films, especially the ones deposited at higher temperature, curve fitting was performed on the XPS core levels. The fitted XPS highresolution spectra are displayed in figure 5. The deconvoluted peaks show the presence of nonstoichiometric oxide (WSe_{2-x}O_x) and carbide species (WSe_{2-x}C_x), located at higher and lower binding energies relative to the W 4f (WSe₂) peaks, respectively, but only present in the 791 °C sample. This could explain the slight variation in terms of PL intensity and peak position in the comparison of the 738 °C and 791 °C samples. By far the lowest FWHM value of the W 4f7/2 and Se 3d5/2 peaks has been determined for the 636 °C sample, indicating a significant increase in crystal quality [70,71]. However, because the low-temperature PL measurements in figure 3a show a higher defect-induced emission for the 636 °C sample than for the 587 °C one, a growth temperature of 587 °C was considered optimal for further investigations.

The impact of the precursor ratio (DiPSe/WCO=1,000, 10,000, 100,000) on the crystal quality of WSe₂ ML domains was investigated with sample series II. The optimum temperature 587 °C from sample series I was used as the growth temperature. The ML coverage of the investigated samples was kept relatively constant at around 50 % by adjusting the growth time accordingly to minimize the impact of BL contribution on the optical properties and maintain consistency (see table 2). Figure 6 shows the SEM images of the WSe₂ ML domains deposited with different DiPSe/WCO ratios. Comparable ML coverage and size of the triangular domains indicate a similar nucleation density. The corresponding low-temperature PL is shown in Figure 7a. The spectra are again normalized to the sapphire PL. Two different excitonic emission features can be distinguished. We assign the most pronounced peak at around 1.7 eV to an overlap of the A exciton X^A (expected to be at around 1.72 eV) and the negative trion emission X⁻ (approximately 30 meV below) ^[59,64,72,73]. The PL at lower energies in figure 7a, as discussed before, indicates defect-induced emission (X^b). The X^b peak is most prominent for a DiPSe/WCO ratio of 1,000, suggesting a high defect density. The inset in figure 7a displays the peak position of the PL maximum as a function of the DiPSe/WCO ratio. It can be seen that the peak position of the PL maximum blue-shifts with increasing DiPSe/WCO ratio. This is an indicator for a smaller contribution of trions and thus less defects, resulting in the PL spectrum being more dominated by A exciton emission at higher energies/lower wavelengths. As the A exciton and trion emissions also overlap with several peaks which can be assigned to sapphire, a reliable fit of the trion peaks is impossible [57]. Therefore, the peak assignments were confirmed by low-temperature reflectivity contrast measurements. Reflectivity contrast is defined as $\Delta R/Rs = (R - Rs)/Rs$, where R is the reflectivity spectrum measured on the sample and Rs denotes the reflectivity spectrum measured on the bare substrate. Figure 7b displays a low-temperature PL spectrum measured at 5.6 K with a laser power density of 28 W/cm² and the reflectivity contrast of the sample with a DiPSe/WCO ratio

of 100,000. The reflectivity measurement was obtained for a sample with a fully coalesced WSe₂ ML with 26 % BL coverage as the series II sample with single domains did not have a sufficiently high reflectance signal (see table 2). It is confirmed that the PL maximum results from an overlap of X^A and a much smaller contribution from X⁻. The strong excitonic nature of the PL of WSe₂ agrees well with literature [74] and indicates a good crystal quality of the samples. Figure 7c displays the power dependence of the peak position of the PL maximum for all DiPSe/WCO ratios. All samples show a blue-shift of the maximum PL peak. The sample with a DiPSe/WCO ratio of 1,000 exhibits the strongest one. As, in contrast to the other samples, this blue-shift is within the spectral range of defectbound excitons. This indicates a strong localization of excitons. For the sample with a DiPSe/WCO ratio of 100,000, the maximum peak position shifts from the peak position of X⁻ to the position of X^A, indicating a saturation of X⁻, thus less defects. This effect is weaker for the sample with a DiPSe/WCO ratio of 10,000. Here, the blue-shift is comparably small and located in the spectral range of X⁻. The PL spectra measured at RT in figure 7d reveal a decrease in PL intensity with a rising DiPSe/WCO ratio. Assuming 1 % absorption for WSe₂ and a radiative lifetime of 0.29 ns ^[75], the exciton density for the PL measurements at RT can be roughly estimated to be about 10¹⁴/cm² for a laser power density of 16 MW/cm². Since EEA processes become dominant in the excitonic dynamics at exciton densities higher than $10^9/\text{cm}^2$ to $10^{12}/\text{cm}^2$ [20,76–78], it can be assumed that the RT PL intensity of our samples is strongly affected by EEA. Because of the smaller defect density for the sample with a DiPSe/WCO ratio of 100,000, the density of defect-bound excitons is lower, i.e. more free excitons are present, which can participate in EEA processes and degrade the PL emission. Compared to sample series I, the XPS results (see figure S1) do reveal neither significant differences between the samples nor additional peaks originating from other species or deviations in stoichiometry.

4. CONCLUSION

We have investigated the impact of the growth temperature and precursor ratio on the crystal quality of WSe₂ ML domains deposited by MOCVD. The samples with a growth temperature between 587 °C and 636 °C exhibit high crystal quality resulting in a low defect-induced PL at low temperatures and high PL at RT. Furthermore, no additional species could be detected by XPS. Increasing the precursor ratio (DiPSe/WCO) from 1,000 up to 100,000 leads to a less defect-dominated PL at low temperatures but also a lower PL intensity at RT at high excitation level. It is shown that the growth temperature generally has a higher influence on the crystal quality of the WSe₂ ML domains than the precursor ratio. In order to achieve a high crystal quality, e.g. low defect density, the WSe₂ domains need to be deposited at temperatures in the range of 587 °C to 636 °C with a precursor ratio of 100,000. Next steps include the deposition of fully coalesced ML at these optimized growth parameters and their implementation in optoelectronic devices.

5. ACKNOWLEDGMENTS

The authors acknowledge the financial support of Deutsche Forschungsgemeinschaft in the frame of the project "Development and analysis of MOCVD growth processes for binary and ternary 2D Transition Metal Dichalcogenides" (VE 5975-1 and BA 1422/21-1) and the Federal Ministry for Education and Research in the Frame of the project "Neurotec II" (16ME0399). In addition, funding was received by the International Max Planck Research School (IMPRS) for Interface Controlled Materials for Energy Conversion (SurMat).

6. REFERENCES

- [1] M. Chhowalla, H. S. Shin, G. Eda, L.-J. Li, K. P. Loh, H. Zhang, *Nature Chemistry* **2013**, *5*, 263.
- [2] A. T. Hanbicki, M. Currie, G. Kioseoglou, A. L. Friedman, B. T. Jonker, *Solid State Communications* **2015**, *203*, 16.
- [3] Z. Li, Y. Xiao, Y. Gong, Z. Wang, Y. Kang, S. Zu, P. M. Ajayan, P. Nordlander, Z. Fang, ACS Nano 2015, 9, 10158.
- [4] O. Lopez-Sanchez, D. Lembke, M. Kayci, A. Radenovic, A. Kis, *Nature Nanotechnology* **2013**, 8, 497.
- [5] W. J. Yu, Y. Liu, H. Zhou, A. Yin, Z. Li, Y. Huang, X. Duan, *Nature Nanotechnology* **2013**, 8, 952.
- [6] W. Zhang, M.-H. Chiu, C.-H. Chen, W. Chen, L.-J. Li, A. T. S. Wee, ACS Nano 2014, 8, 8653.
- [7] B. W. H. Baugher, H. O. H. Churchill, Y. Yang, P. Jarillo-Herrero, *Nature Nanotechnology* **2014**, *9*, 262.
- [8] D. Andrzejewski, H. Myja, M. Heuken, A. Grundmann, H. Kalisch, A. Vescan, T. Kümmell, G. Bacher, *ACS Photonics* **2019**, *6*, 1832.
- [9] J. S. Ross, P. Klement, A. M. Jones, N. J. Ghimire, J. Yan, D. G. Mandrus, T. Taniguchi, K. Watanabe, K. Kitamura, W. Yao, D. H. Cobden, X. Xu, *Nature Nanotechnology* **2014**, *9*, 268.
- [10] F. Withers, O. Del Pozo-Zamudio, A. Mishchenko, A. P. Rooney, A. Gholinia, K. Watanabe, T. Taniguchi, S. J. Haigh, A. K. Geim, A. I. Tartakovskii, K. S. Novoselov, *Nature Materials* **2015**, *14*, 301.
- [11] H. Fang, S. Chuang, T. C. Chang, K. Takei, T. Takahashi, A. Javey, *Nano Letters* **2012**, *12*, 3788.
- [12] B. Radisavljevic, A. Radenovic, J. Brivio, V. Giacometti, A. Kis, *Nature Nanotechnology* **2011**, 6, 147.
- [13] S. Tongay, J. Suh, C. Ataca, W. Fan, A. Luce, J. S. Kang, J. Liu, C. Ko, R. Raghunathanan, J. Zhou, F. Ogletree, J. Li, J. C. Grossman, J. Wu, *Scientific Reports* **2013**, *3*, 2657.
- [14] H. Qiu, T. Xu, Z. Wang, W. Ren, H. Nan, Z. Ni, Q. Chen, S. Yuan, F. Miao, F. Song, G. Long, Y. Shi, L. Sun, J. Wang, X. Wang, *Nature Communications* **2013**, *4*, 2642.
- [15] H. Nan, Z. Wang, W. Wang, Z. Liang, Y. Lu, Q. Chen, D. He, P. Tan, F. Miao, X. Wang, J. Wang, Z. Ni, *ACS Nano* **2014**, *8*, 5738.
- [16] Z. Cao, M. Harb, S. Lardhi, L. Cavallo, *The Journal of Physical Chemistry Letters* **2017**, 8, 1664.
- [17] L. Feng, J. Su, D. Li, Z. Liu, Physical Chemistry Chemical Physics 2015, 17, 6700.
- [18] J. Hong, Z. Hu, M. Probert, K. Li, D. Lv, X. Yang, L. Gu, N. Mao, Q. Feng, L. Xie, J. Zhang, D. Wu, Z. Zhang, C. Jin, W. Ji, X. Zhang, J. Yuan, Z. Zhang, *Nature Communications* 2015, 6, 6293.
- [19] J. Lu, A. Carvalho, X. K. Chan, H. Liu, B. Liu, E. S. Tok, K. P. Loh, A. H. Castro Neto, C. H. Sow, *Nano Letters* **2015**, *15*, 3524.
- [20] M. Zhou, W. Wang, J. Lu, Z. Ni, Nano Research 2021, 14, 29.
- [21] V. Carozo, Y. Wang, K. Fujisawa, B. R. Carvalho, A. McCreary, S. Feng, Z. Lin, C. Zhou, N. Perea-López, A. L. Elías, *Science advances* **2017**, *3*, e1602813.
- [22] Y.-C. Lin, T. Björkman, H.-P. Komsa, P.-Y. Teng, C.-H. Yeh, F.-S. Huang, K.-H. Lin, J. Jadczak, Y.-S. Huang, P.-W. Chiu, *Nature Communications* **2015**, *6*, 1.
- [23] W. Zhou, X. Zou, S. Najmaei, Z. Liu, Y. Shi, J. Kong, J. Lou, P. M. Ajayan, B. I. Yakobson, J.-C. Idrobo, *Nano Letters* **2013**, *13*, 2615.

- [24] D. Yang, X. Fan, F. Zhang, Y. Hu, Z. Luo, Nanoscale research letters 2019, 14, 192.
- [25] J. Ye, Y. An, H. Yan, J. Liu, Applied Surface Science 2019, 497, 143788.
- [26] Z. Lin, B. R. Carvalho, E. Kahn, R. Lv, R. Rao, H. Terrones, M. A. Pimenta, M. Terrones, *2D Mater.* **2016**, *3*, 22002.
- [27] Y. J. Zheng, Y. Chen, Y. L. Huang, P. K. Gogoi, M.-Y. Li, L.-J. Li, P. E. Trevisanutto, Q. Wang, S. J. Pennycook, A. T. S. Wee, S. Y. Quek, ACS Nano 2019, 13, 6050.
- [28] H.-P. Komsa, A. V. Krasheninnikov, Phys. Rev. B 2015, 91.
- [29] L. Li, E. A. Carter, Journal of the American Chemical Society 2019, 141, 10451.
- [30] G. Moody, K. Tran, X. Lu, T. Autry, J. M. Fraser, R. P. Mirin, L. Yang, X. Li, K. L. Silverman, *Physical review letters* **2018**, *121*, 57403.
- [31] H. Wang, C. Zhang, F. Rana, Nano Letters 2015, 15, 339.
- [32] K. Chen, R. Ghosh, X. Meng, A. Roy, J.-S. Kim, F. He, S. C. Mason, X. Xu, J.-F. Lin, D. Akinwande, S. K. Banerjee, Y. Wang, *npj 2D Mater Appl* **2017**, *1*.
- [33] Z. Wu, Z. Luo, Y. Shen, W. Zhao, W. Wang, H. Nan, X. Guo, L. Sun, X. Wang, Y. You, *Nano Research* **2016**, *9*, 3622.
- [34] Z. Wu, W. Zhao, J. Jiang, T. Zheng, Y. You, J. Lu, Z. Ni, *The Journal of Physical Chemistry C* **2017**, *121*, 12294.
- [35] R. Kaupmees, M. Grossberg, M. Ney, A. Asaithambi, A. Lorke, J. Krustok, *Phys. Status Solidi RRL* **2020**, *14*, 1900355.
- [36] S. Mouri, Y. Miyauchi, M. Toh, W. Zhao, G. Eda, K. Matsuda, *Phys. Rev. B* **2014**, *90*, 155449.
- [37] M. Amani, P. Taheri, R. Addou, G. H. Ahn, D. Kiriya, D.-H. Lien, J. W. Ager, R. M. Wallace, A. Javey, *Nano Letters* **2016**, *16*, 2786.
- [38] M. Amani, D.-H. Lien, D. Kiriya, J. Xiao, A. Azcatl, J. Noh, S. R. Madhvapathy, R. Addou, S. Kc, M. Dubey, *Science* **2015**, *350*, 1065.
- [39] L. Yuan, T. Wang, T. Zhu, M. Zhou, L. Huang, *The Journal of Physical Chemistry Letters* **2017**, *8*, 3371.
- [40] H. Liu, C. Wang, Z. Zuo, D. Liu, J. Luo, Advanced Materials 2020, 32, 1906540.
- [41] Z. G. Yu, Y.-W. Zhang, B. I. Yakobson, *Nano Letters* **2015**, *15*, 6855.
- [42] D. H. Lee, Y. Sim, J. Wang, S.-Y. Kwon, APL Materials 2020, 8, 30901.
- [43] H. Y. Jeong, Y. Jin, S. J. Yun, J. Zhao, J. Baik, D. H. Keum, H. S. Lee, Y. H. Lee, *Advanced materials (Deerfield Beach, Fla.)* **2017**, *29*.
- [44] Y. Nie, C. Liang, K. Zhang, R. Zhao, S. M. Eichfeld, P.-R. Cha, L. Colombo, J. A. Robinson, R. M. Wallace, K. Cho, 2D Mater. 2016, 3, 25029.
- [45] S. M. Eichfeld, L. Hossain, Y.-C. Lin, A. F. Piasecki, B. Kupp, A. G. Birdwell, R. A. Burke, N. Lu, X. Peng, J. Li, A. Azcatl, S. McDonnell, R. M. Wallace, M. J. Kim, T. S. Mayer, J. M. Redwing, J. A. Robinson, *ACS Nano* **2015**, *9*, 2080.
- [46] M.-H. Shang, H. Hou, J. Zheng, Z. Yang, J. Zhang, S. Wei, X. Duan, W. Yang, *The Journal of Physical Chemistry Letters* **2018**, *9*, 6032.
- [47] M. Marx, A. Grundmann, Y.-R. Lin, D. Andrzejewski, T. Kümmell, G. Bacher, M. Heuken, H. Kalisch, A. Vescan, *Journal of Elec Materi* **2018**, *47*, 910.
- [48] D. A. Shirley, *Phys. Rev. B* **1972**, *5*, 4709.
- [49] X. Zhang, T. H. Choudhury, M. Chubarov, Y. Xiang, B. Jariwala, F. Zhang, N. Alem, G.-C. Wang, J. A. Robinson, J. M. Redwing, *Nano Letters* **2018**, *18*, 1049.
- [50] M. Ohring, The materials science of thin films, Academic Press, Boston 1992.
- [51] S. M. Eichfeld, V. O. Colon, Y. Nie, K. Cho, J. A. Robinson, 2D Mater. 2016, 3, 25015.

- [52] T. Kwak, J. Lee, B. So, U. Choi, O. Nam, Journal of Crystal Growth 2019, 510, 50.
- [53] B. Liu, M. Fathi, L. Chen, A. Abbas, Y. Ma, C. Zhou, ACS Nano 2015, 9, 6119.
- [54] E. Del Corro, H. Terrones, A. Elias, C. Fantini, S. Feng, M. an Nguyen, T. E. Mallouk, M. Terrones, M. A. Pimenta, *ACS Nano* **2014**, *8*, 9629.
- [55] H. Terrones, E. Del Corro, S. Feng, J. M. Poumirol, D. Rhodes, D. Smirnov, N. R. Pradhan, Z. Lin, M. A. T. Nguyen, A. L. Elías, T. E. Mallouk, L. Balicas, M. A. Pimenta, M. Terrones, Scientific Reports 2014, 4, 4215.
- [56] S. Mignuzzi, A. J. Pollard, N. Bonini, B. Brennan, I. S. Gilmore, M. A. Pimenta, D. Richards, D. Roy, *Phys. Rev. B* **2015**, *91*.
- [57] T. Han, H. Liu, S. Wang, S. Chen, W. Li, X. Yang, M. Cai, K. Yang, *Nanomaterials (Basel, Switzerland)* **2019**, *9*.
- [58] S. Park, N. Mutz, T. Schultz, S. Blumstengel, A. Han, A. Aljarb, L.-J. Li, E. J. W. List-Kratochvil, P. Amsalem, N. Koch, *2D Mater.* **2018**, *5*, 25003.
- [59] Y.-C. Lin, B. Jariwala, B. M. Bersch, K. Xu, Y. Nie, B. Wang, S. M. Eichfeld, X. Zhang, T. H. Choudhury, Y. Pan, R. Addou, C. M. Smyth, J. Li, K. Zhang, M. A. Haque, S. Fölsch, R. M. Feenstra, R. M. Wallace, K. Cho, S. K. Fullerton-Shirey, J. M. Redwing, J. A. Robinson, ACS Nano 2018, 12, 965.
- [60] M. Manca, M. M. Glazov, C. Robert, F. Cadiz, T. Taniguchi, K. Watanabe, E. Courtade, T. Amand, P. Renucci, X. Marie, G. Wang, B. Urbaszek, *Nature Communications* **2017**, *8*, 14927.
- [61] S. Tongay, J. Suh, C. Ataca, W. Fan, A. Luce, J. S. Kang, J. Liu, C. Ko, R. Raghunathanan, J. Zhou, F. Ogletree, J. Li, J. C. Grossman, J. Wu, *Scientific Reports* **2013**, *3*, 2657.
- [62] A. Srivastava, M. Sidler, A. V. Allain, D. S. Lembke, A. Kis, A. Imamoğlu, *Nature Nanotechnology* **2015**, *10*, 491.
- [63] T. Yan, X. Qiao, X. Liu, P. Tan, X. Zhang, Applied Physics Letters 2014, 105, 101901.
- [64] X. Zhang, F. Zhang, Y. Wang, D. S. Schulman, T. Zhang, A. Bansal, N. Alem, S. Das, V. H. Crespi, M. Terrones, J. M. Redwing, *ACS Nano* **2019**, *13*, 3341.
- [65] Q. Zhang, C. H. Naylor, Z. Gao, R. Wu, I. H. Abidi, M.-Q. Zhao, Y. Ding, A. A. Cagang, M. Zhuang, X. Ou, Z. Luo, ACS Nano 2017, 11, 10808.
- [66] Y. Park, S. W. Han, C. C. S. Chan, B. P. L. Reid, R. A. Taylor, N. Kim, Y. Jo, H. Im, K. S. Kim, *Nanoscale* **2017**, *9*, 10647.
- [67] J. A. Robinson, B. Schuler, Applied Physics Letters 2021, 119, 140501.
- [68] J. R. Shallenberger, Surf. Sci. Spectra 2018, 25, 14001.
- [69] S. Subramanian, N. Briggs, J. Shallenberger, M. T. Wetherington, J. A. Robinson, *J. Mater. Res.* **2020**, *35*, 855.
- [70] S. Bertolazzi, S. Bonacchi, G. Nan, A. Pershin, D. Beljonne, P. Samorì, *Advanced materials* (*Deerfield Beach, Fla.*) **2017**, *29*.
- [71] M. Timpel, G. Ligorio, A. Ghiami, L. Gavioli, E. Cavaliere, A. Chiappini, F. Rossi, L. Pasquali, F. Gärisch, E. J. W. List-Kratochvil, P. Nozar, A. Quaranta, R. Verucchi, M. V. Nardi, *npj 2D Mater Appl* **2021**, *5*.
- [72] J. Jadczak, J. Kutrowska-Girzycka, P. Kapuściński, Y. S. Huang, A. Wójs, L. Bryja, *Nanotechnology* **2017**, *28*, 395702.
- [73] A. M. Jones, H. Yu, N. J. Ghimire, S. Wu, G. Aivazian, J. S. Ross, B. Zhao, J. Yan, D. G. Mandrus, Di Xiao, W. Yao, X. Xu, *Nature Nanotechnology* **2013**, *8*, 634.
- [74] G. Wang, A. Chernikov, M. M. Glazov, T. F. Heinz, X. Marie, T. Amand, B. Urbaszek, *Rev. Mod. Phys.* **2018**, *90*.

- [75] M. Palummo, M. Bernardi, J. C. Grossman, Nano Letters 2015, 15, 2794.
- [76] S. Mouri, Y. Miyauchi, M. Toh, W. Zhao, G. Eda, K. Matsuda, *Phys. Rev. B* 2014, 90.
- [77] D. Sun, Y. Rao, G. A. Reider, G. Chen, Y. You, L. Brézin, A. R. Harutyunyan, T. F. Heinz, *Nano Letters* **2014**, *14*, 5625.
- [78] P. D. Cunningham, K. M. McCreary, B. T. Jonker, *The Journal of Physical Chemistry Letters* **2016**, *7*, 5242.

Table 1 Characteristics of sample series I. Variation of growth temperature.

T _{growth} [°C]	DiPSe/WCO	t _{growth} [min]	ML coverage [%]	Domain size [nm]
537	1,000	45	69.7 ± 1.9	26 ± 8
587	1,000	45	61.7 ± 2.6	46 ± 7
636	1,000	45	52.8 ± 0.9	56 ± 6
688	1,000	45	47.4 ± 2.6	64 ± 7
738	1,000	45	53.2 ± 2.5	69 ± 6
791	1,000	45	45.1 ± 2.7	95 ± 12

Table 2 Characteristics of sample series II. Variation of the precursor ratio (DiPSe/WCO) at 587 °C growth temperature. The molar precursor fluxes of WCO and DiPSe as well as the growth time (t_{growth}) and the monolayer (ML) coverage and domain size are given.

DiPSe/WCO	WCO flow [nmol/min]	DiPSe flow [μmol/min]	t _{growth} [min]	ML coverage [%]	Domain size [nm]
1,000	259	259	45	54.5 ± 3.5	41 ± 5
10,000	35	349	45	49.0 ± 3.2	41 ± 4
100,000	4	448	15	45.9 ± 1.2	40 ± 5

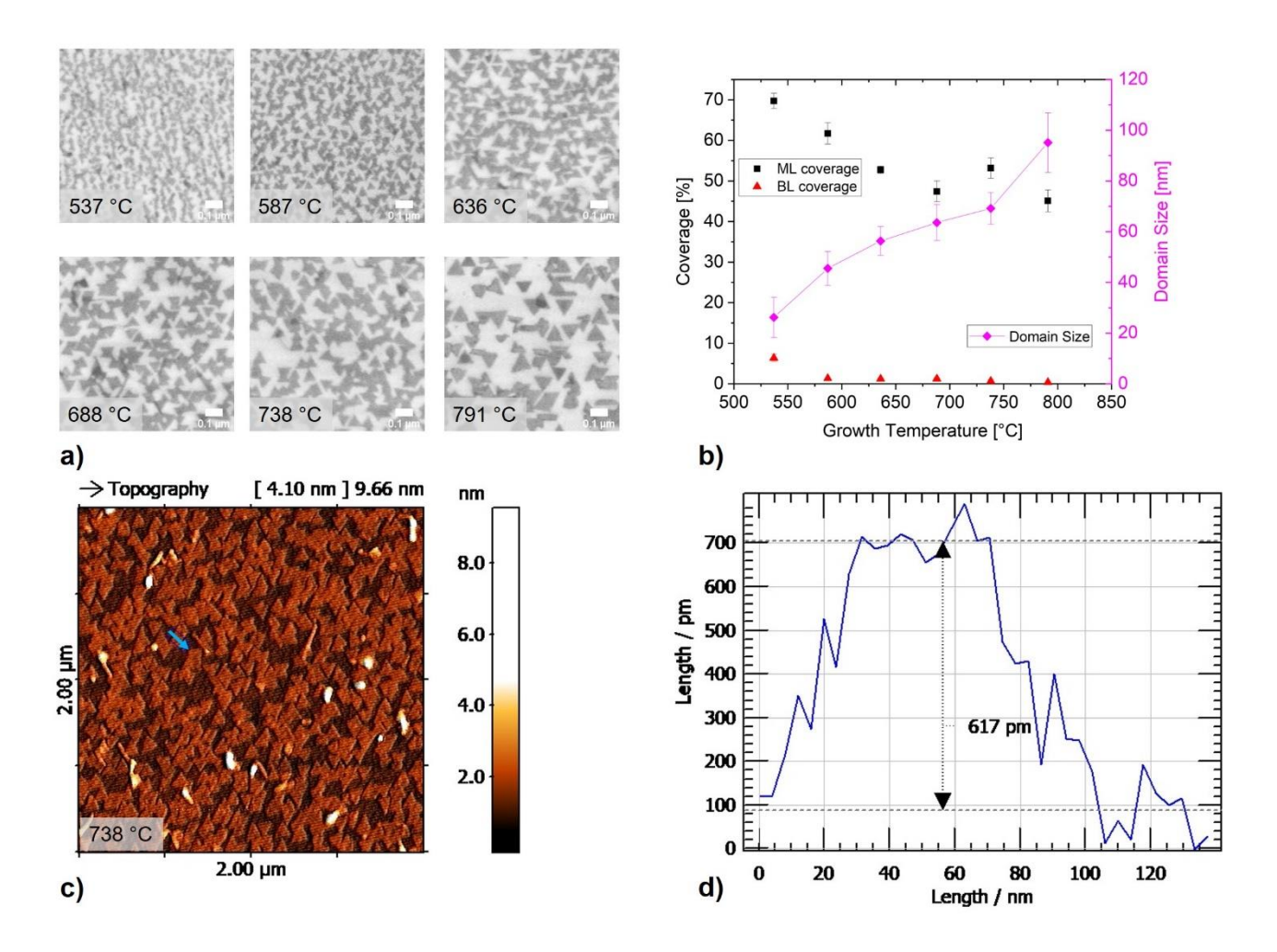


Figure 1. (a) SEM images of WSe₂ ML domains grown on sapphire substrates with different surface temperatures ranging from 537 °C to 791 °C. (b) The average ML, BL coverage and domain size of

the as-grown WSe_2 at the respective surface temperatures. (c) AFM image of the 738 °C sample surface. The blue arrow marks the linescan of the height profile of a WSe_2 ML domain shown in (d). RMS as a function of growth temperature for sample series I.

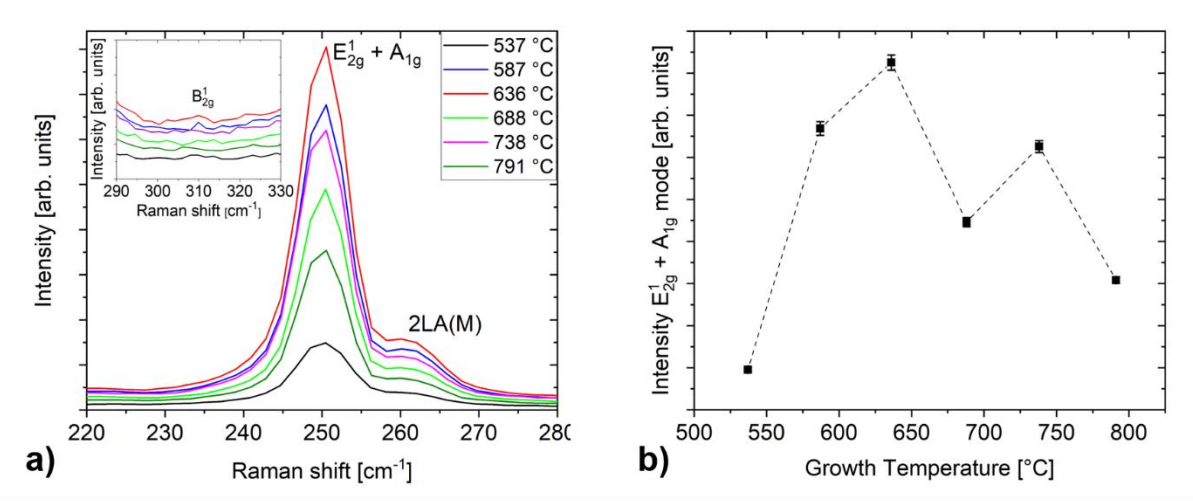


Figure 2. (a) Raman spectra in the range of the two first-order Raman modes E^{1}_{2g} and A_{1g} . The inset displays the Raman spectra in the region of the interlayer breathing mode at 310 cm⁻¹. (b) Intensity of E^{1}_{2g} and A_{1g} mode as a function of growth temperature. The intensity was fitted by a Lorentzian in OriginLab.

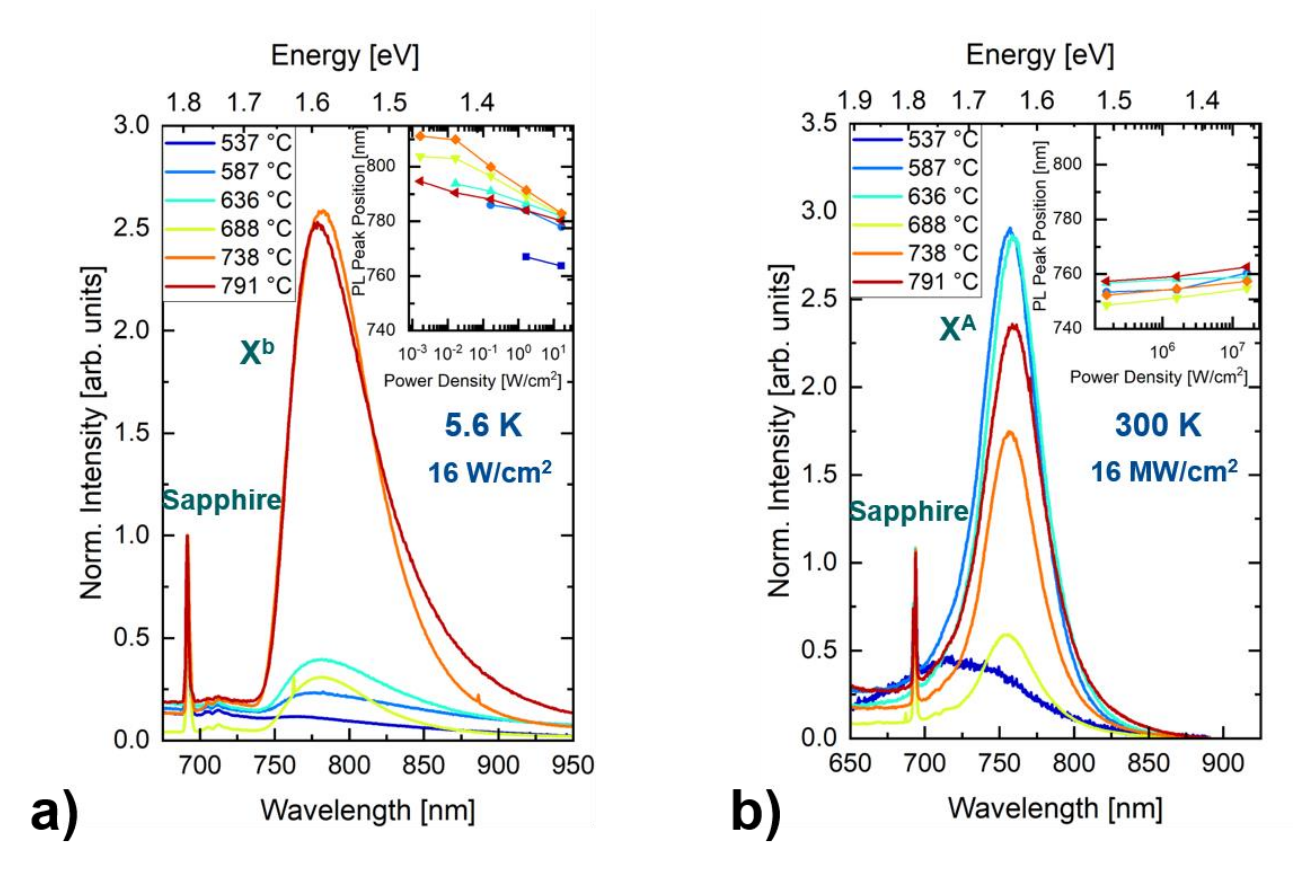


Figure 3. PL spectra measured at 5.6 K (a) and RT (b) for growth temperatures ranging from 537 °C to 791 °C. Inset: PL peak position as a function of the power density.

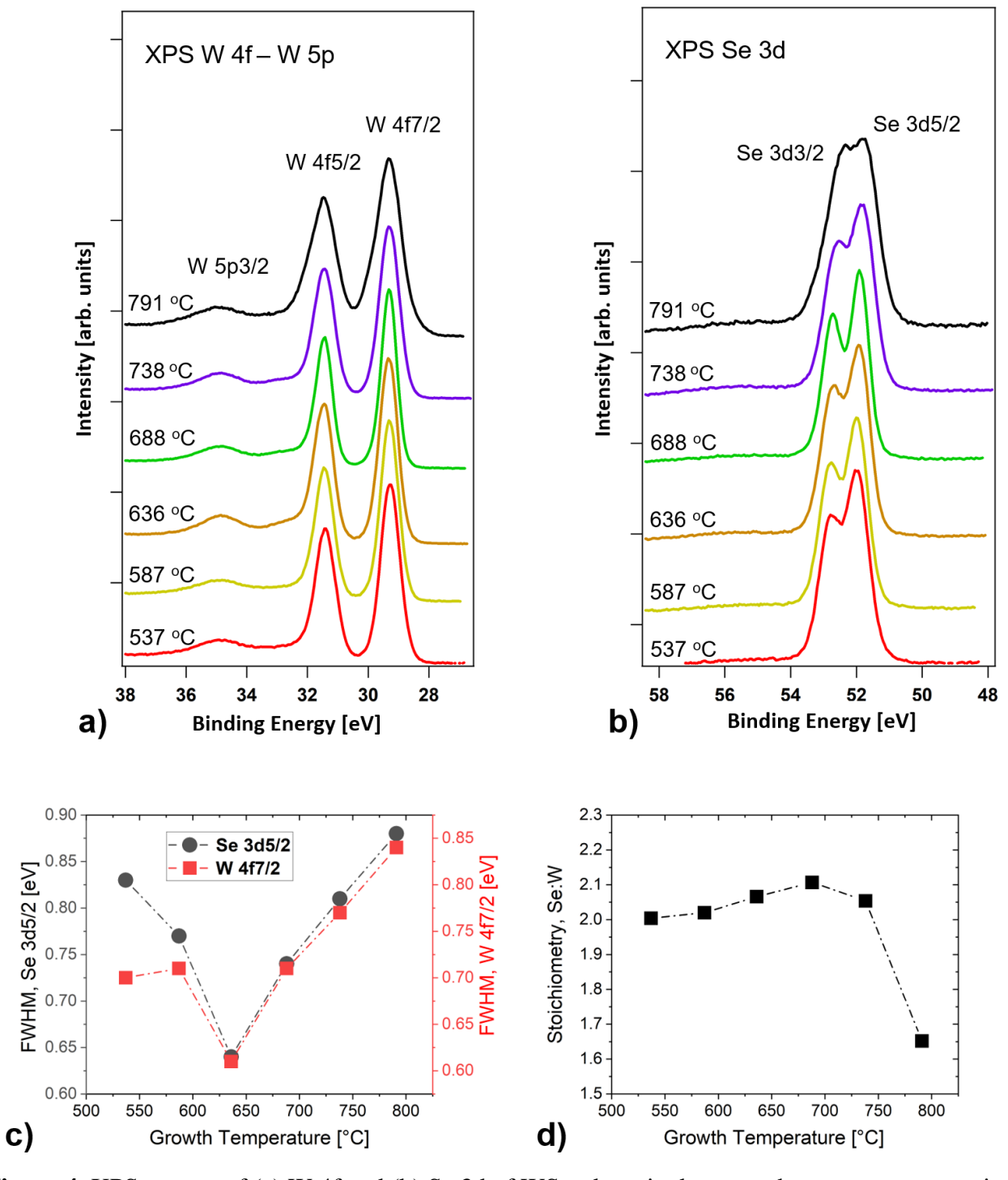


Figure 4. XPS spectra of (a) W 4f and (b) Se 3d of WSe₂ deposited at growth temperatures ranging from 537 $^{\circ}$ C to 791 $^{\circ}$ C. c) FWHM of the W 4f7/2 and Se 3d5/2 peak and d) the stoichiometry as a function of growth temperature.

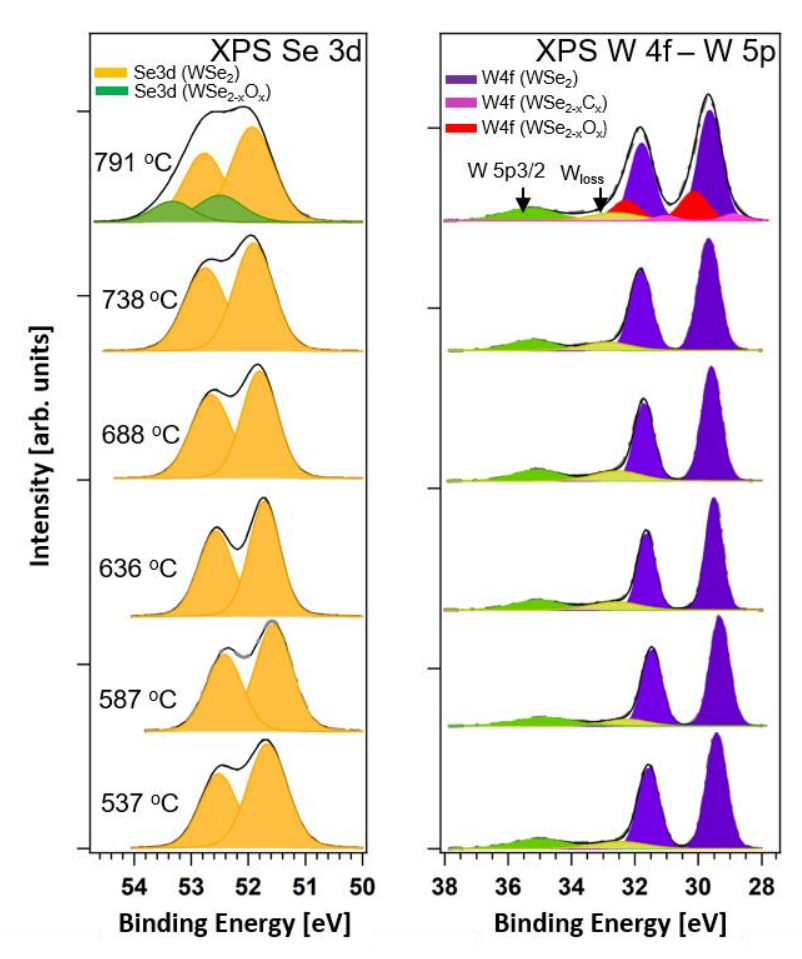


Figure 5. Fitted XPS spectra of Se 3d (left) and W 4f (right) of WSe₂ deposited at growth temperatures ranging from 537 °C to 791 °C.

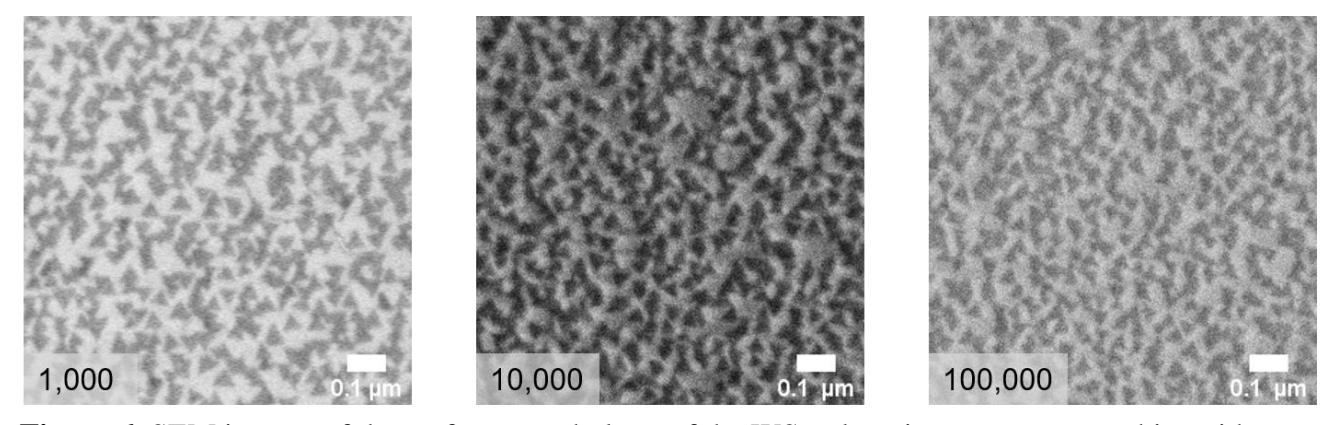


Figure 6. SEM images of the surface morphology of the WSe₂ domains grown on sapphire with a precursor ratio of DiPSe/WCO=1,000, 10,000 and 100,000. (b) ML coverage and domain size as a function of the precursor ratio (DiPSe/WCO).

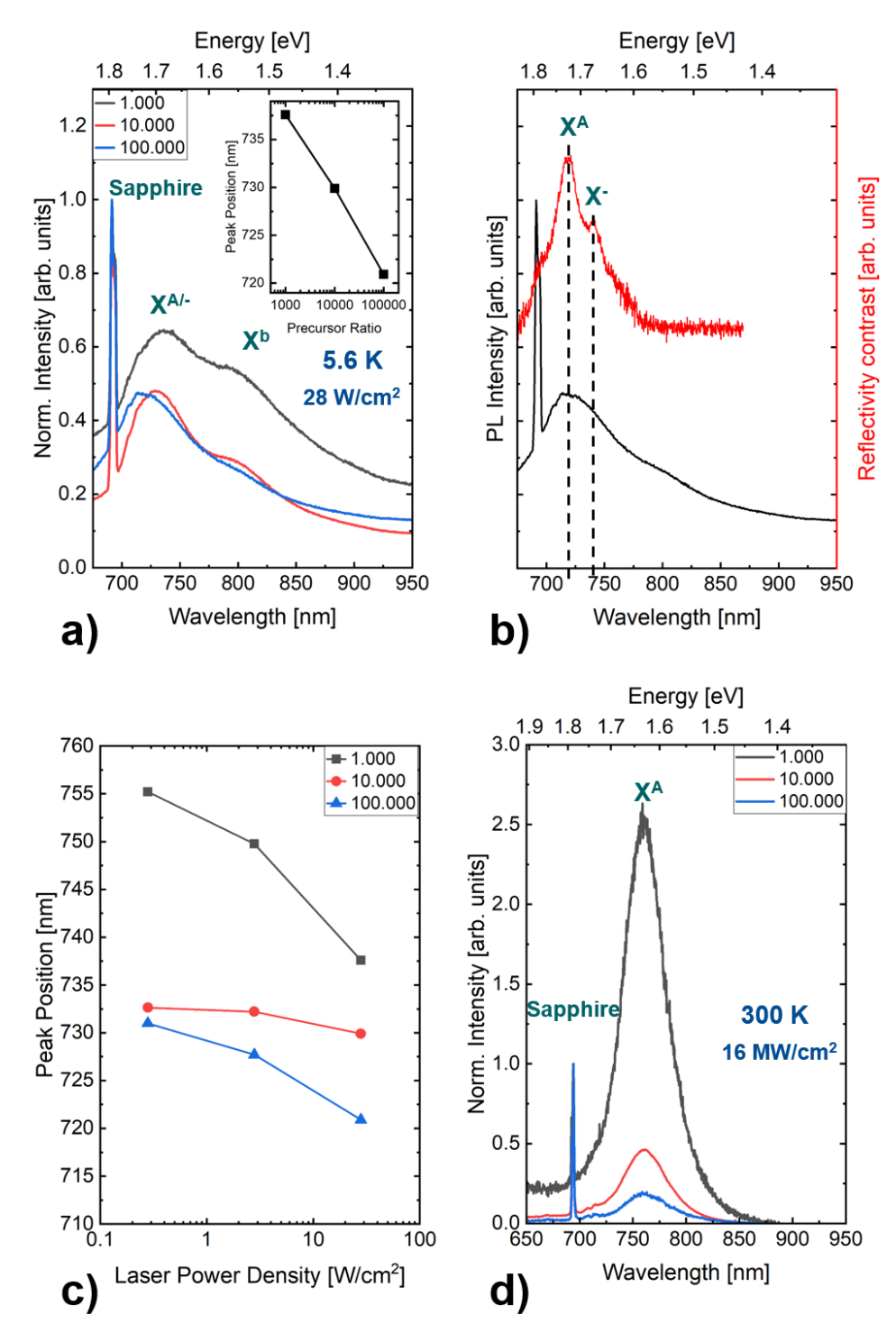


Figure 7. (a) PL spectra measured at 5.6 K for precursor ratios DiPSe/WCO=1,000, 10,000 and 100,000. The inset shows the position of the PL maximum as a function of precursor ratio. (b) PL spectra measured at 5.6 K and reflectivity contrast measured at 9.5 K of WSe₂ deposited with a precursor ratio of DiPSe/WCO=100,000. X^A indicates the A exciton and X⁻ the negative trion. (c)

Position of PL maximum as a function of laser power density at 5.6 K and (d) PL spectra measured at RT for precursor ratios DiPSe/WCO=1,000, 10,000 and 100,000.